This is the accepted version of the article: Liu, Yu et al. "Solution-based synthesis and processing of Sn- and Bi-doped Cu_3SbSe_4 nanocrystals, nanomaterials and ring-shaped thermoelectric generators" in Journal of Materials Chemistry A, Vol. 5, Issue 6 (February 2017), p. 2592-2602. Available at: 10.1039/c6ta08467b. This article version is "all rights reserved" http://www.europeana.eu/rights/rr-f/

Solution-Synthesis and Processing of Sn- and Bi-Doped Cu_3SbSe_4 Nanocrystals, Nanomaterials and Ring-Shaped Thermoelectric Generators

Yu Liu,[a] Silvia Ortega,[a,b] Doris Cadavid,*[,a] Maria Ibáñez,[c,d] Lili Xi,[e] Jonathan De Roo,[f,g] Antonio M. López,[h] Sara Martí,[i] Ignasi Cabezas,[b,h] María Mata,[i] Zhishan Luo,[a] Chaochao Dun,[j] Oleksandr Dobrozhan,[a] Wenqing Zhang,[e] José Martins,[g] Maksym V. Kovalenko,[c,d] Jordi Arbiol,[i,k] German Noriega,*[,b] Ji-Ming Song,*[,l] and Andreu Cabot*[,a,k]

[a] Catalonia Institute for Energy Research-IREC, 08930 Sant Adrià del Besos (Barcelona), Spain
[b] Cidete Ingenieros S.L. Anselm Clavé 98, 08800 Vilanova i la Geltrú, Barcelona, Spain
[c] Institute of Inorganic Chemistry, Department of Chemistry and Applied Biosciences, ETH Zürich, CH-8093, Switzerland
[d] Empa-Swiss Federal Laboratories for Materials Science and Technology, Dübendorf, CH-8600, Switzerland
[e] Shanghai Institute of Ceramics, Chinese Academy of Sciences, Shanghai, 200050, China
[f] Department of Inorganic and Physical Chemistry, Ghent University, B-9000 Ghent, Belgium
[g] Department of Organic and Marcromolecular Chemistry, Ghent University, B-9000 Ghent, Belgium
[h] Departament d'Enginyeria Electrónica, Universitat Politècnica de Catalunya, EPSEVG, Av.Victor Balaguer s/n, Spain
[i] Catalan Institute of Nanoscience and Nanotechnology (ICN2), CSIC and The Barcelona Institute of Science and Technology (BIST), Campus UAB, Bellaterra, 08193 Barcelona, Spain
[j] Center for Nanotechnology and Molecular Materials Wake Forest University, 501 Deacon Blvd. Winston Salem NC 27105 USA
[k] ICREA, Pg. Lluís Companys 23, 08010 Barcelona, Spain
[l] School of Chemistry & Chemical Engineering, Anhui University, Hefei, Anhui, 230601, P. R. China

ABSTRACT

Copper-based chalcogenides, comprising abundant, low-cost, and environmental friendly elements, are excellent materials for several energy conversion applications, including photocatalysis, electrocatalysis, photovoltaics and thermoelectrics. In such applications, the production of either crystalline thin films or bulk nanomaterials with high surface area or high relative density by solution-processed nanocrystals (NCs) provides several potential advantages, such as high material yield and throughput and composition control with unmatched spatial resolution and low cost. Here we report on the production of Cu_3SbSe_4 (CASe) NCs with tuned amounts of Sn^{4+} and Bi^{5+} dopants. After proper ligand removal, as monitored by nuclear magnetic resonance and infrared spectroscopies, these NCs were used as building blocks to produce dense CASe bulk nanomaterials for solid state thermoelectric (TE) energy conversion. By adjusting the amount of extrinsic dopants, dimensionless TE figures of merit (ZT) up to 1.26 at 673 K were obtained. Such high ZT values are related to an optimized carrier concentration by proper doping, a minimized lattice thermal conductivity due to efficient phonon

scattering at point defects and grain boundaries, and to an increase of the Seebeck coefficient obtained by a modification of the band structure with the Bi doping. These materials were further employed to fabricate ring-shaped TE generators to be coupled to hot pipes and which provide 20 mV and 1 mW per TE element when exposed to a 160 ºC temperature gradient.

1. INTRODUCTION

Tetrahedrally coordinated copper-based chalcogenides have emerged as a realistic alternative material for a number of energy conversion applications, including photovoltaics, photocatalysis and thermoelectricity.[1-7] Beyond the best studied ternary and quaternary Cu-Ga-In,[8-10] Cu-Zn-Sn,[11-15] Cu-Zn-Ge[16,17] chalcogenides, I−V−VI tetrahedrally coordinated semiconductors remain largely underexplored. In particular, CASe is a semiconductor with a relatively small direct band gap of 0.3 eV and a defect-related carrier density on the order of 10^{18} cm^{-3} at ambient temperatures.[18] It crystallizes in a zinc blende-type tetragonal superstructure that can be considered as a three-dimensional Cu-Se framework of distorted [$CuSe_4$] tetrahedra with inserted one dimensional array of [$SbSe_4$] tetrahedra. It features two Cu sites with different Cu-Se bond lengths. The valence band maximum is mainly formed by a hybridization of Cu-3d and Se-4p states, while the conduction band minimum is dominated by Sb-5s and Se-4p hybridization. Therefore, the Cu-Se framework provides avenues for hole transport with relatively high mobility, up to 135 $cm^2V^{-1}s^{-1}$ for undoped and 49 $cm^2V^{-1}s^{-1}$ for highly doped materials.[19-21] Furthermore, such a complex lattice structure is prohibits the phonon propagation, resulting in advantageously low thermal conductivities. The high hole mobility and the low phonon mean free path, combined with an appropriate electronic band structure (including a large degeneracy at the valence band maximum[19, 20]) render CASe an excellent TE material. However, to maximize its TE performance, it is strictly necessary to optimize its charge carrier concentration. Either the density of *intrinsic* defects that control hole concentration is adjusted or an *extrinsic* p-type dopant is introduced, preferably in the non-conducting sub-lattice to minimize the adverse effects on the hole mobility.

Nanocrystal-based, bottom-up strategies offer several advantages to produce thin films, porous or dense nanostructured materials for semiconductor-based, energy conversion applications. From an engineering viewpoint, the unmatched compositional and interfacial control makes this route very robust and versatile, allowing to establish structure-property relationships and subsequently enabling the rational design of superior materials. From a practical viewpoint, facile and inexpensive solution synthesis and processing allows for a low-cost and high throughput production with high material yield.[22-27] However, two major challenges with colloidal nanomaterials are (i) the incorporation of controlled amounts of electronic dopants and (ii) the removal of organics. Both of them are critical for optimizing the semiconductive properties of the final nanostructured material.[26]

Thus far, colloidal Cu_3SbS_4[28-30] and $Cu_{12}Sb_4S_{13}$[29-31] NCs have been primarily used for photoelectrochemical studies and a few attempts to produce nanostructured bulk CASe have been reported. However, bottom-up strategies to efficiently and cost-effectively produce CASe materials and CASe-based devices remains to be demonstrated. [32, 33] Here, we report a solution-based, scalable

synthesis approach to produce several grams of monodisperse CASe NCs, doped with controlled amounts of Sn and Bi. We demonstrate their bottom-up processing into high density bulk nanostructured materials with high TE performances. We further use this material to fabricate TE rings, which potentially provide improved thermal contact for heat recovery from pipes.

2. MATERIALS AND METHODS

Chemicals and solvents. Copper (I) chloride (CuCl, ⩾99%), antimony (III) chloride ($SbCl_3$, 99%), bismuth (III) acetate ($Bi(CH_3CO_2)_3$, >99.99%), selenium powder (99.5%), ammonium thiocyanate (NH_4SCN, ⩾99%), dodecanethiol (DDT, 98%), 1-octadecene (ODE, technical grade 90%), oleic acid (OA, technical grade 99%), decanoic acid (DDAc, ⩾98%), and oleylamine (OLA, technical grade 70%) were purchased from Sigma Aldrich. Tin (II) chloride ($SnCl_2$, 98%) was purchased from Strem. Analytical grade methanol, ethanol and chloroform were obtained from various sources. All chemicals were used as received without further purification.

Selenium precursor solution. Selenium powder (23.688 g, 300 mmol) was dissolved in 300 ml OLA and 300 ml DDT at room temperature, cycled between vacuum and argon to remove the oxygen in the flask, and then stirred under argon atmosphere until Se powder was completely dissolved.

Synthesis of Cu_3SbSe_4 NCs. In a typical synthesis, 10.0 mmol CuCl, 4.0 mmol $SbCl_3$,15 ml OLA, 10 ml OA and 100 ml ODE were mixed in a 500 ml three-neck flask and stirred for 20 min at room temperature . The solution was kept at 130 ºC under vacuum and vigorous stirring for 30 min, and then heated to 180 ºC. The color of the solution changed from light green to yellowish-brown at the temperature of over 170 ºC. 50 ml of selenium precursor solution was swiftly injected into the reaction under magnetic stirring and the color of the solution changed immediately from brown to dark green, indicating that the nucleation and subsequent growth of CASe NCs occurred. After injection, the temperature of the reaction mixture dropped to ~165 °C, and it was allowed to recover to the pre-injection temperature (180 °C). The overall reaction time after recovering to 180 °C was 30 min, and then the sample was rapidly cooled to room temperature through water bath. NCs were collected by precipitation with ethanol. The final product could be well dispersed in non-polar solvents such as toluene or chloroform, forming a stable, dark-green dispersion (inset of Fig S1b). For subsequent chemical, structural and functional characterization, NCs were purified by multiple precipitation (6000 rpm for 5 min) and redispersion steps using chloroform as solvent and ethanol as non-solvent. The resulting powder was re-suspended in chloroform and stored for subsequent characterization and use. This synthesis protocol was optimized to produce more than 2.0 g of NCs per batch (Figure S1a), which was the amount of material required for a complete characterization of the material at the laboratory scale, including the fabrication of a ring-shaped device.

Synthesis of $Cu_3Sb_{1-x}Sn_xSe_4$, $Cu_3Sb_{1-x}Bi_xSe_4$ and $Cu_3Sb_{1-x-y}Sn_xBi_ySe_4$ NCs. Sn and Bi-doped CASe NCs were produced following the above procedure, but replacing the desired amount of $SbCl_3$ by $SnCl_2$ and/or $Bi(CH_3CO_2)_3$.

Ligand removal. The $Cu_3Sb_{1-x}Sn_xSe_4$, $Cu_3Sb_{1-x}Bi_xSe_4$ and $Cu_3Sb_{1-x-y}Sn_xBi_ySe_4$ NCs produced in each

batch were divided into 6 centrifuge tubes (~350 mg in 10 ml of chloroform in each tube). In each of the tubes, 2 ml of a 50 mM NH_4SCN solution in acetone was added. Then the solution was shaked during 1~2 min to displace the organic ligands attached to the NC surface, followed by precipitation of the NCs by centrifugation. This process was repeated several times, adding chloroform and NH_4SCN in each step. Finally, NCs were precipitated and dried under vacuum to obtain a fine powder.

Bulk nanomaterial consolidation. The dried NCs were loaded into a graphite die and compacted into pellets (Ø10 mm×~1.5 mm). The process was carried out in Ar atmosphere, using a custom-made hot press to simultaneously apply a pressure of 70 MPa and a temperature of 643-653 K during 30 min. In this system, the heat is provided by an induction coil operated at 30-80 KHz and it is applied directly to a graphite die acting as a susceptor. Fast heating ramps of 20 ºC/second are reached by this method with a 25 kW induction heater. The relative densities of the pressed pellets were measured by the Archimedes' method and found to be always higher than 87% of the theoretical values.

Ring thermoelectric generators. TE rings with an internal diameter of 28 mm and an external diameter of 39 mm were fabricated by placing the nanopowder between two concentrically placed copper rings and hot-pressing the material at a temperature of 643-653 K during 30 min and 20 MPa of pressure using an especially designed detachable die.

Structural and chemical characterization. Crystallographic phases were characterized by powder X-ray diffraction (XRD, 2θ angle: 20° to 80°; scanning rate: 1°/min) on a Bruker AXS D8 ADVANCE X-ray diffractometer with Cu–Kα radiation (λ= 0.15406 Å). X-ray photoelectron spectroscopy (XPS) was performed on a VG ESCA scientific theta probe spectrometer in constant analyzer energy mode with a pass energy of 28 eV and Al K α (1486.6 eV) radiation as the excitation source. Size and shape of initial NCs were examined by transmission electron microscopy (TEM) using a ZEISS LIBRA 120, operating at 120 kV. High resolution TEM (HRTEM) images were obtained using a Jeol 2010F field-emission gun microscope with a 0.19 nm point-to-point resolution at 200 keV with an embedded Gatan image filter for EELS analyses. The morphology of the hot-pressed pellets was characterized using field-emission scanning electron microscopy (SEM, Auriga Zeiss) at 5.0 kV. The NC composition was analyzed by inductive plasma spectroscopy (ICP, Elementar Analysensyteme Gmbh, Germany) and an Oxford energy dispersive X ray spectrometer (EDX) attached to Zeiss Auriga SEM. Fourier-transform infrared spectroscopy (FTIR) were acquired by using an Alpha Bruker FTIR spectrometer with the platinum attenuated total reflectance (ATR) single reflection module.

NMR. Nuclear Magnetic Resonance (NMR) measurements were recorded on a Bruker Avance III Spectrometer operating at a ^1H frequency of 500.13 MHz and equipped with a BBI-Z probe. The sample temperature was set to 298.2 K. One dimensional (1D) ^1H and 2D NOESY (Nuclear Overhauser Effect Spectroscopy) spectra were acquired using standard pulse sequences from the Bruker library; zg and noesygpphpp respectively. For the quantitative 1D ^1H measurements, 64k data points were sampled with the spectral width set to 16 ppm and a relaxation delay of 30 sec. The NOESY mixing time was set to 300 ms, with 2048 data points sampled in the direct dimension for 512 data points in the indirect dimension, with the spectral width set to 11.5 ppm. For 2D processing, the spectra were zero filled to a 4096×2048 real data matrix, followed by multiplication with squared

cosine bell function in both dimensions prior to Fourier transformation. The 1D spectra were apodized with an exponential window function. Concentrations were obtained using the Digital ERETIC method. Diffusion measurements (2D DOSY) were performed using a double stimulated echo sequence (dstegp2s)[34] for convection compensation and with monopolar gradient pulses.[34] Smoothed rectangle gradient pulse shapes were used throughout. The gradient strength was varied linearly from 2-95% of the probe's maximum value (calibrated at 50.2 G/cm) in 64 steps, with the gradient pulse duration and diffusion delay optimized to ensure a final attenuation of the signal in the final increment of less than 10% relative to the first increment. The diffusion coefficients were obtained by fitting the Stejskal-Tanner (ST) equation to the signal intensity decay. For the pulse sequence at hand, the appropriate ST equation is: [35]

$$I = I_0 e^{-(\gamma\delta g\xi)^2 D(\Delta - 0.6\delta)} \quad (0)$$

with the gyromagnetic ratio of the observed ^{1}H nucleus γ, the gradient pulse length δ, the gradient strength g, the diffusion time Δ and the diffusion coefficient D. The shape factor ξ depends on the gradient shape but this is usually already corrected for in the gradient strength value by the Bruker software, TOPSPIN. The ST equation for other pulse programs is only slightly different and the impact on the diffusion coefficient is very small in the case of long diffusion times (Δ>250 ms). In a real DOSY experiment, values of Δ and δ are set while varying g to derive the decay curve.[35]

Thermoelectric property measurement. Seebeck coefficients were measured by using a static DC method. Electrical resistivity data was obtained by a standard four-probe method. Both the Seebeck coefficient and the electrical resistivity were measured simultaneously in a LSR-3 LINSEIS system in the temperature range between room temperature and 673 K, under helium atmosphere. The thermal conductivity was calculated by $\kappa = \lambda C_p \rho$, where λ is the thermal diffusivity, C_p is the heat capacity, and ρ is the mass density of the specimen. A XFA 600 Xenon Flash Apparatus was used to determine the thermal diffusivities of the samples. The specific heat (C_p) was measured by means of the differential scanning calorimeter method (DSC model T2000 TA Instruments), and the density (ρ) values used here were calculated using the Archimedes' method.

Hall measurement. The carrier concentration and mobility were measured using the Hall measurement system (PPMS-9T, Quantum Design Inc., USA) at room temperature under a magnetic field of 2 T. Values provided correspond to an average of 5 consecutive measurements

Device test. TE rings were tested in a custom-made test station. Temperature was monitored by two thermocouples attached at the copper electrodes and the open circuit voltage was measured by a Keithley 2400. A heating cartridge was used to rise the temperature of the internal part of the ring, while the external part of the ring was kept at low temperature by means of TE coolers. The maximum temperature reached at the hot side was 250 ºC. At this point the temperature at the cold side was 90 ºC, what provided a maximum temperature gradient of 160 ºC.

Density Functional Theory (DFT). Since traditional Generalized Gradient Approximation (GGA) methods always underestimate semiconductors band gaps, in this work, the electronic structures were calculated by a mBJ method[44-46] implemented in the Vienna ab initio Simulation Package (VASP), and

adopting an effective Coulomb U (U_{eff}= U- J) of 4 eV for the Cu-3d states.[47] Because the doping level was small, the defect system was modeled by creating a 2*2*2 supercell. The calculations were done starting from a 64 atom (24 Cu, 12 Sb and 32 Se for pure system and 24 Cu, 11 Sb, 1 Bi, 32 Se for doping system).

3. RESULTS AND DISCUSSION

CASe NCs were produced from copper chloride, antimony chlorides and selenium powder dissolved in OLA and DDT, as detailed in the experimental part. This synthesis protocol possesses a high batch-to-batch reproducibility and a 94% material yield. Figure 1 and S2 shows representative TEM and HRTEM micrographs with the respective indexed power spectrum of the 18±2 nm CASe NCs produced following the procedure here described. The NC crystallographic phase was identified as tetragonal CASe (space group $I\bar{4}2m$ (121), Table S1) with lattice constants a=b=0.566 nm and c=1.128 nm, which is in agreement with XRD data (Figure 2a, JCPDS card No. 85-0003). No secondary phases were detected by HRTEM and XRD analysis. Within their experimental error, ICP and EDX showed the metal and chalcogenide ratios to match that of stoichiometric CASe (Cu_3SbSe_4, Figure S4). Electron Energy Loss Spectroscopy (EELS) was used for compositional analysis within each particle using Sb $M_{4,5}$, Cu $L_{2,3}$ and Se $L_{2,3}$ edges. In the central region of the NC, elemental quantification showed the presence of around 12% Sb, 30% Cu and 48% Se, which is compatible with the CASe stoichiometry. In the outer part of the NCs, the relative composition of Sb and Cu were found to be higher than in the core and that of Se was slightly lower: 17 % Sb, 40% Cu and 43% Se (Figure S3).

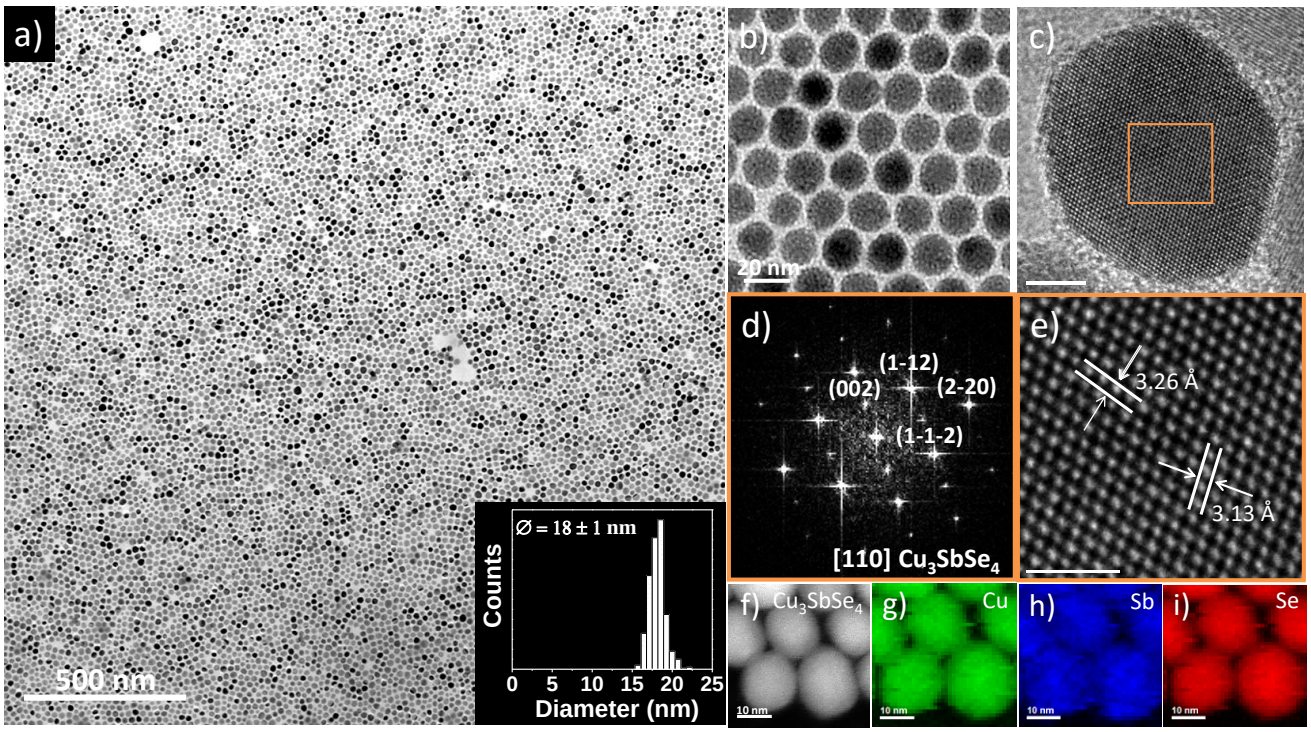

Figure 1. (a) Representative TEM micrograph of the CASe NCs. The inset shows the histogram for the measured particle size distribution (18±2 nm). (b) A higher-magnification TEM micrograph; (c)

HRTEM image of a single CASe NCs. (d) Its respective power spectrum fitting with CASe tetragonal phase. (e) the detail of the squared regions of the single CASe NCs. (f) High-angle annular dark field scanning TEM (HAADF-STEM) image of some CASe NCs and (g)-(i) areal density of the three elements.

Similar to CASe NCs, $Cu_3Sb_{1-x}Sn_xSe_4$ (Figure S6), $Cu_3Sb_{1-x}Bi_xSe_4$ (Figure S7) and $Cu_3Sb_{1-x-y}Sn_xBi_ySe_4$ (Figure S8) NCs showed quasi-spherical morphologies with an average size of around 18 nm. However, increasingly broader size and shape distributions were obtained as the amount of doping was increased (Figures S6 and S7). Doped CASe NCs were characterized by larger a and c lattice parameters, as evidenced by a slight XRD peak shift toward lower angles in the XRD patterns displayed in Figure 2b, c and d. The lattice expansion is attributed to the substitution of Sb^{5+} (0.6 Å) by the larger Sn^{4+} (0.69 Å) and/or Bi^{5+} (0.76 Å) cations.[20] Figure S9 and Table S2-S4 display the elemental composition of Sn and Bi-doped CASe as obtained by EDX.

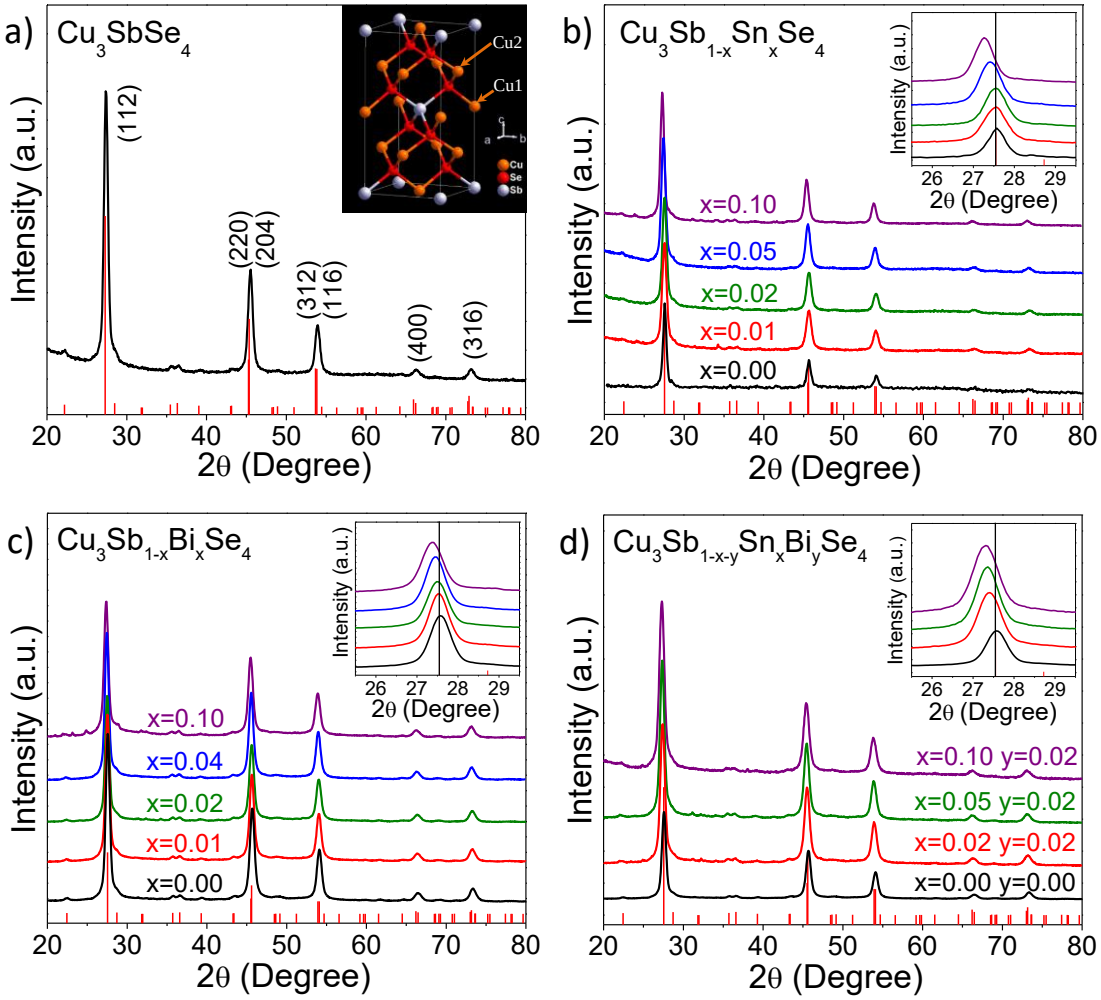

Figure 2. (a) XRD pattern of CASe NCs including the reference pattern JCPDS 85-0003. The inset shows a unit cell of tetragonal CASe. (b) XRD patterns of $Cu_3Sb_{1-x}Sn_xSe_4$ (x=0.00, 0.01, 0.02, 0.05, 0.10) NCs. (c) XRD patterns of $Cu_3Sb_{1-x}Bi_xSe_4$ (x=0.00, 0.01, 0.02, 0.04, 0.10) NCs. (d) XRD patterns

of $Cu_3Sb_{1-x-y}Sn_xBi_ySe_4$ (x=0.02, 0.05, 0.10 and y=0.02) NCs. Insets in graphs b)-c) show a detail of the (112) peak, at around 2θ =27.5°.

CASe NCs were synthesized in the presence of OLA, OA and DDT. In order to identify which surfactants were present on the NC surface and establish their bonding nature, NMR analysis was performed. Figure 3a shows a ^{1}H NMR spectrum of the as synthetized NCs (unpurified) and the ^{1}H NMR spectrum of NCs purified four times by precipitation/redispersion with acetonitrile as non-solvent and toluene as solvent. In the spectrum of unpurified NCs we observe the characteristic resonances of a *terminal* alkene at 5.0 and 5.8 ppm, associated to ODE. The resonance around 5.5 ppm is associated with an *internal* alkene, from OLA and/or OA. The ODE resonances possess fine structure, indicating the unbound nature of ODE. In contrast, the alkene resonance is a superposition of sharp and broad resonances, associated with free and bound ligands respectively.[36] After purification, the ODE features disappear completely together with the majority of the sharp resonance corresponding to the free molecules OLA or OA, indicating a successful purification of the NCs solution. Further purification to remove the remaining free ligand in solution render the NCs completely insoluble in any solvent. The NOESY spectrum (Figure S10) contains negative (black) nOe cross peaks confirming the interaction of OLA/OA with the surface. [36] To discriminate whether OLA or OA (or both) is stabilizing the NC surface, we reproduced the exact same synthesis described above but instead of OA we used dodecanoic acid (DDAc). Although DDAc and OA are both fatty acids and are expected to interact identically with NC surfaces, DDAc has no alkene group and this allows us to distinguish OLA from OA. Figure 3b shows the NMR spectra of CASe NPs synthetized with DDAc. Since the ^{1}H NMR spectra are almost identical to spectra of the dispersions prepared with OA and because OLA is now the only molecule with an alkene resonance, we identify OLA as a ligand. Additionally, the intensity of the alkene resonance and CH_3 resonance features a 2:3 ratio. This excludes any other (fully saturated) ligands such as DDT or DDAc, proving that OLA is the only ligand present. Since OLA is an L-type ligand and the NCs were found to be stoichiometric (*vide supra*), this NC system belongs to the earlier established class of binding motifs; NC(L). To assess the dynamics of interaction, Diffusion Ordered NMR Spectroscopy (DOSY) experiments were performed. A good fitting of the CH_3 signal decay was only obtained with two exponentials, indicating two populations (Figure S11). The small fraction with a high diffusion coefficient (552 $\mu m^2/s$) is attributed to free OLA while the fraction with a low diffusion coefficient (45 $\mu m^2/s$) is associated with bound OLA. Using the Stokes-Einstein equation, a solvodynamic diameter of 16.5 nm is calculated from the diffusion coefficient. Since this is close to the diameter from TEM (16-20 nm), we conclude that OLA is firmly attached to the NC surface and diffuses together with the NC. Considering the L-type nature of OLA,[37] it is usually involved in a more dynamic stabilization of the NC surface.[38] However, it was repeatedly reported that Cu-based NCs typically have tightly bound amines bound to the surface.[13, 39] It should however be noted that OLA is quite easily desorbed during purification suggesting only a moderate binding affinity for the NC surface, in line with L-type ligand behavior.

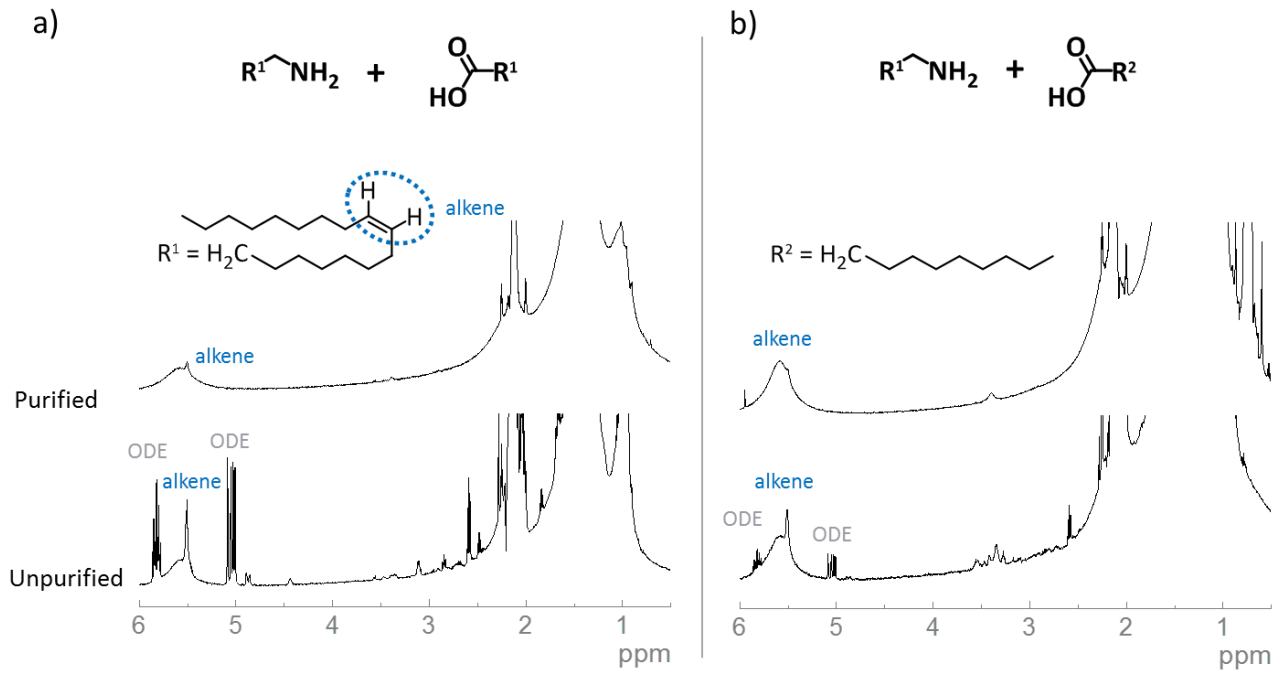

Figure 3. ^{1}H NMR spectrum of CASe 18±2 nm NPs synthesized with a) OA and b) DDAc shown before (bottom) and after (top) purification.

To facilitate charge transport/transfer, CASe NCs were thoroughly purified by multiple precipitation/re-dispersion steps and subsequently treated with NH_4SCN to completely displace remaining organic ligands. Figure S12 shows FTIR spectra of dried CASe NCs before (CASe–OL) and after (CASe–LD) organic ligand displacement with a 50 mM NH_4SCN solution. CASe–OL spectrum showed the characteristic features of OLA: C–H vibration modes have a strong band in the high-frequency region (2850–3000 cm^{-1}) and various peaks in the lower frequency region, between 700 cm^{-1} and 1650 cm^{-1}. These features completely disappeared from the CASe–LD spectrum, proving the effective organic ligand displacement.

Nanocrystalline disk-shaped CASe pellets (Ø10 mm×~1.5 mm) were prepared under Ar atmosphere by hot-pressing around 700 mg of ligand-displaced NCs at ~650 K, 70 MPa and for 30 min. The pellets had a metallic luster and were mechanically robust enough to endure a polishing process. Relative densities above 87% of the theoretical value were measured for all samples. XRD analysis of the undoped and doped CASe pellets showed no crystallographic or related compositional change after the hot-press process, nor the appearance of secondary phases (Figure S13). During the hot-press treatment, CASe NCs coalesced to form larger crystalline domains with sizes ranging from tens to few hundred nanometers (Figure S14).

The electrical conductivity (σ), Seebeck coefficient (S), thermal conductivity (κ), and the dimensionless TE figure or merit $ZT= \sigma S^2T/\kappa$ of undoped and Sn- and Bi-doped CASe pellets are displayed in Figures 4, 5 and 7. Undoped CASe nanomaterials were characterized by relatively low σ, which increased with temperature up to 6.2×10^3 Sm^{-1}, and positive S in the

whole temperature range measured. Significantly higher σ, up to 9.0×10^4 Sm^{-1} at room temperature, were obtained for Sn-doped CASe, which showed a degenerated semiconductor behavior with a decrease of σ with temperature. On the contrary, S decreased with the Sn introduction. The observed increase of σ and decrease of S with the amount of Sn indicate Sn ions to play a p-type doping electronic role within CASe. This electronic role was confirmed by a one order of magnitude increase in the measured Hall charge carrier concentration with the Sn introduction, from $p=5x10^{18}$ cm^{-3} in CASe to $p=9x10^{19}$ cm^{-3} in $Cu_3Sb_{0.98}Sn_{0.02}Se_4$. Overall, higher power factors ($PF = \sigma S^2$) were obtained for the doped samples, with a maximum PF of 1.14 $mWm^{-1}K^{-2}$ at 673 K for the sample containing a 2% replacement of Sb by Sn, $Cu_3Sb_{0.98}Sn_{0.02}Se_4$ (Figure S15a). Relatively low thermal conductivities, which as expected decreased with temperature, were obtained for all the analyzed materials. For undoped CASe, in the temperature range from 327 K to 653 K, κ dropped from 1.60 $Wm^{-1}K^{-1}$ to 0.81 $Wm^{-1}K^{-1}$, which are lower values than those previously reported for bulk CASe,[19, 20, 40, 41] but slightly higher than those reported for nanostructured CASe produced by co-precipitation,[32] and much higher than the estimated minimum κ (0.26 $Wm^{-1}K^{-1}$).[42, 43] Lower lattice thermal conductivities (κ_L) were obtained with the incorporation of Sn due to the introduced lattice distortion and the increased density of point defects (Figure S15b). However, the associated increase of the electronic contribution to the thermal conductivity (κ_e) resulted in an overall increase of κ for most of the Sn-doped CASe (Figure 4c). Overall, ZT significantly increased with the introduction of relatively small amounts of Sn, reaching ZT=0.97 at 673 K for $Cu_3Sb_{0.98}Sn_{0.02}Se_4$, which represents more than a 2-fold increase over undoped CASe.

The CASe nanocrystalline material showed a good stability even when heated and maintained at relatively high temperatures for long periods of time. Figure S20 shows the results obtained from 5 consecutive heating-cooling cycles. Minor differences can be observed from cycle to cycle and mainly from the first cycle to the following ones. To account for the minor variations obtained from the first to the following cycles, all samples were measured at least 3 consecutive times and results from the first cycle were discarded. Figure 4e shows the results obtained from $Cu_3Sb_{0.9}Sn_{0.1}Se_4$ during a 55 h test involving the heating of the sample from 323 to 626 K at a rate of 10 K/min and then maintaining the sample at 656 K for 54 h. During this time, the electrical conductivity and Seebeck coefficient changed by just ~1% and ~3%, respectively.

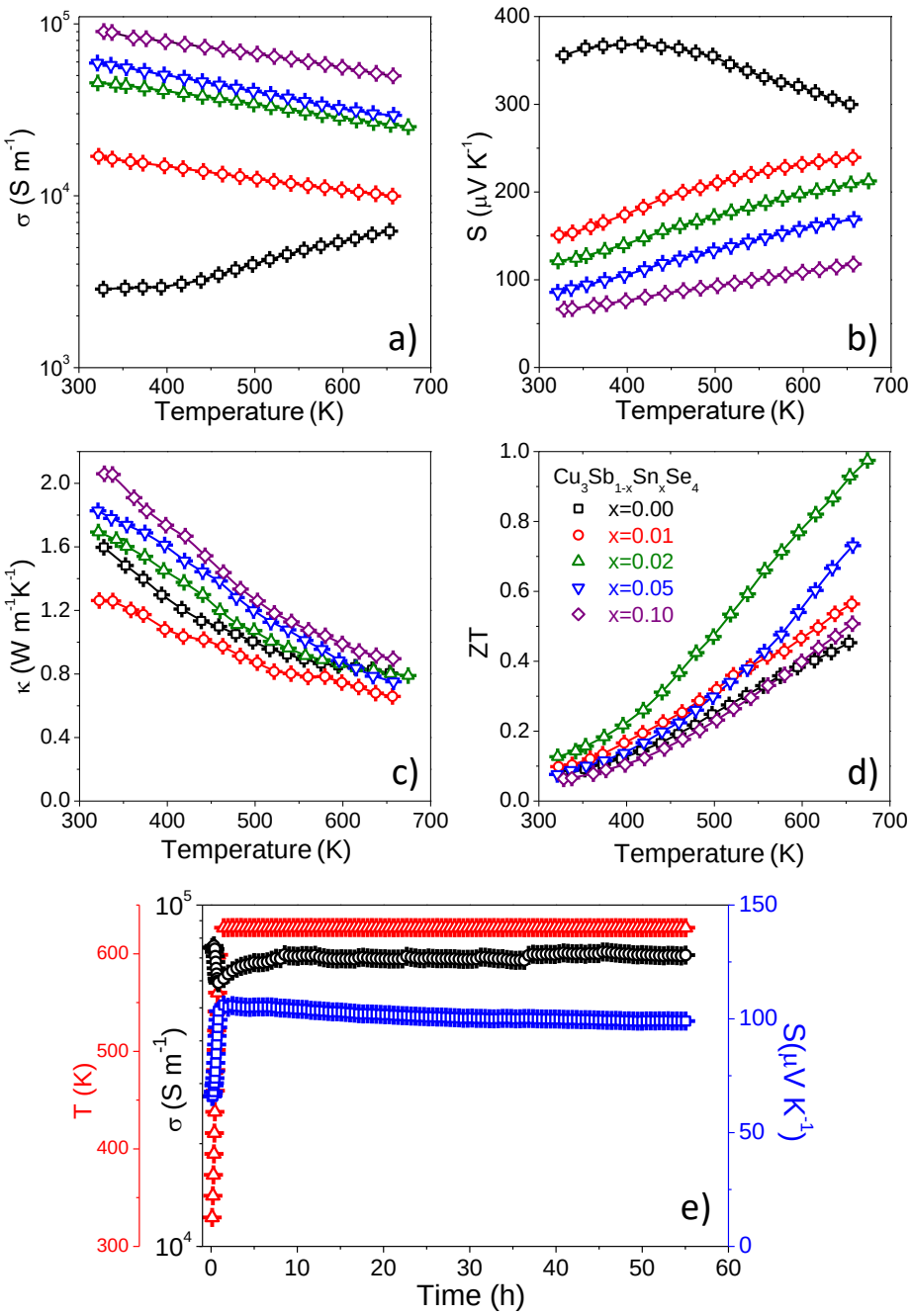

Figure 4. a-d) Temperature dependence of (a) electric conductivity (σ), (b) Seebeck coefficient (S), (c) thermal conductivity (κ), and (d) The figure of merit (ZT) of $Cu_3Sb_{1-x}Sn_xSe_4$ (x=0.01, 0.02, 0.05 and 0.10). e) Time evolution of the electrical conductivity (σ, ○), Seebeck coefficient (S, □) and temperature (T, △) of $Cu_3Sb_{0.9}Sn_{0.1}Se_4$ during a 55 h test.

When replacing part of the Sb^{5+} by isovalent Bi^{5+}, slightly lower σ were obtained (Figure 5a). Hall charge carrier concentration measurements provided slightly lower hole concentrations for Bi-CASe samples when compared with CASe, but always on the same order of magnitude. A slight decrease in the charge carrier concentration could be associated to an indirect diminution of the

concentration of an intrinsic defect that acts as a p-type dopant, e.g. the presence of Cu^{1+} at Sb^{5+} sites, Cu or Sb vacancies or an overall excess of Se. However, significantly larger S values were measured for all Bi-CASe samples (Figure 5b), which did not correlated well with the small decrease in electrical conductivity when just taking into account a slight modification of the charge carrier concentration.

To further determine the possible influence of Bi in the electron energy band structure of CASe, DFT calculations were carried out. Figure 6 shows the band structure of pure CASe and Bi-doped compounds. Results indicate that pure CASe is a semiconductor with a direct band gap of 0.238 eV, which is consistent with previous data.[47] Both the valence band maximum (VBM) and the conduction band minimum (CBM), which mainly determines electronic transport properties in a p-type semiconductor such as CASe, are mainly composed of Cu d and Se p electrons (Figure S18 and S19). While the substitution of Bi atoms for Sb had little effect on the band structure at the CBM, it significantly affected the VBM decreasing the band gap and resulting in a divergence of the multi-valleys bands, which could result in a reduction of a bipolar effect on the Seebeck coefficient. Additional modelling is being carried out to further discern the origin of this Seebeck coefficient increase and to determine the optimum composition to maximize it.

Combining σ with S, the highest PF values for Bi-CASe were obtained with a composition $Cu_3Sb_{0.98}Bi_{0.02}Se_4$ (~0.77 $mWm^{-1}K^{-2}$ at 608 K, Figure S16). Bi-doped CASe were characterized by lower κ than CASe due to slightly lower κ_e and κ_L contributions. Overall, higher ZT values, up to 0.81 for $Cu_3Sb_{0.98}Bi_{0.02}Se_4$ at 648 K, were obtained for Bi-CASe when compared with CASe. However, lower PF and overall ZT were calculated for Bi-CASe than for Sn-CASe mainly due to the lower electrical conductivities of the former. While Bi doping was demonstrated to result in a modification of the energy band structure that resulted in higher Seebeck coefficients, Sn-doping allowed optimizing the charge carrier concentration, which is key to maximize ZT.

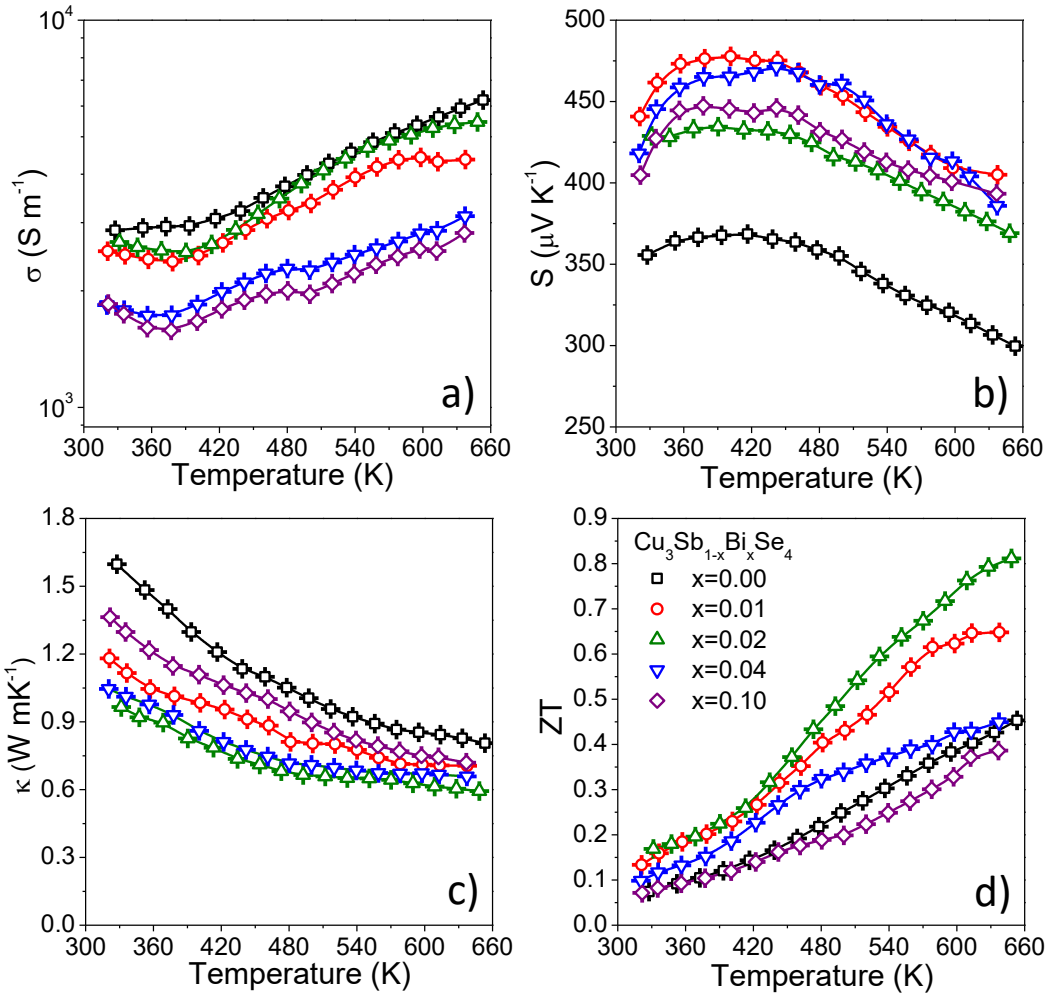

Figure 5. Temperature dependence of (a) electric conductivity (σ), (b) Seebeck coefficient (S), (c) thermal conductivity (κ), and (d) the figure of merit (ZT) of $Cu_3Sb_{1-x}Bi_xSe_4$ (x=0.01, 0.02, 0.04 and 0.10).

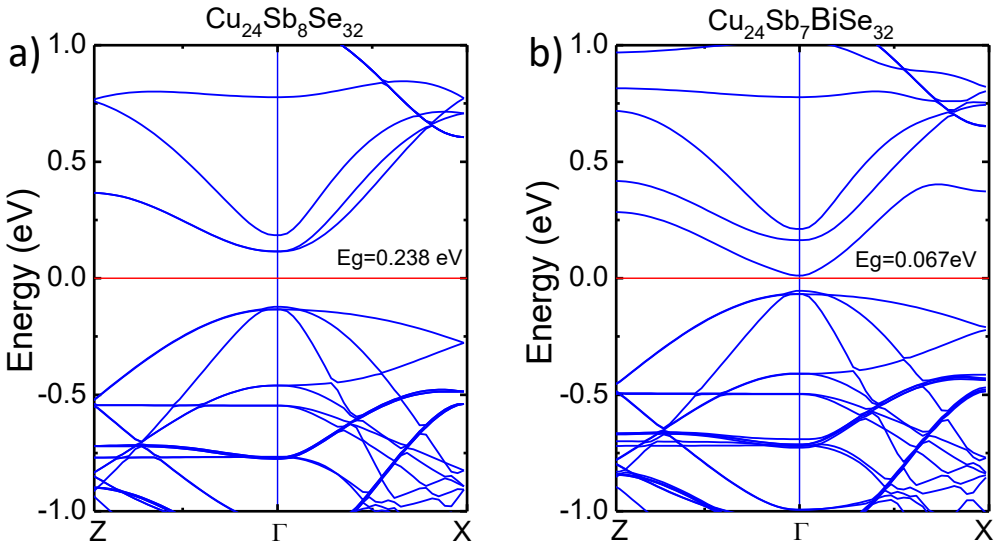

Figure 6. Electronic band structure of pristine CASe and Bi-CASe.

To take advantage of the carrier concentration control that a p-type dopant such as Sn provides and of the convenient increase of S resulting from the Bi presence, we prepared a series of CASe samples simultaneously doped with both elements. Figure 7 shows the temperature dependence of the electrical and thermal transport properties of $Cu_3Sb_{0.98-x}Sn_xBi_{0.02}Se_4$ (x = 0.02, 0.05 and 0.10). These samples showed a degenerated electrical conductivity behavior, associated to a large level of doping. σ increased with the Sn content as with Sn-CASe. Surprisingly, σ of co-doped Sn,Bi-CASe was actually larger than that of Sn-CASe samples with the same amount of Sn, which Hall measurements associated to a slight increase of the charge carrier concentration, up to $p=1x10^{20}$ cm^{-3}. On the other hand, S decreased for all Sn,Bi-CASe co-doped samples when compared with plain CASe due to the large increase of charge carrier concentration. However, S values of co-doped materials slightly increased when compared with Sn-doped CASe with equivalent electrical conductivities, proving the positive effect of the Bi addition. Overall, the PFs of co-doped Sn,Bi-CASe were significantly higher than those of Sn- or Bi-CASe, and reached up to ~1.81 $mWm^{-1}K^{-2}$ at 654 K for $Cu_3Sb_{0.88}Sn_{0.10}Bi_{0.02}Se_4$ (Figure S17a). Like in the case of Sn-CASe, in Sn,Bi-CASe the dependence of κ with the dopant concentration showed a competition between the decrease of κ_L associated with the increased lattice defects and the increase of κ_e associated to the much higher electrical conductivities (Figures 7c and S17d). Overall, ZT values up to 1.26 at 673K were obtained for $Cu_3Sb_{0.88}Sn_{0.10}Bi_{0.02}Se_4$, which is among the best ZT values obtained with a Pb- and Te-free material in this middle temperature range (Table S5).

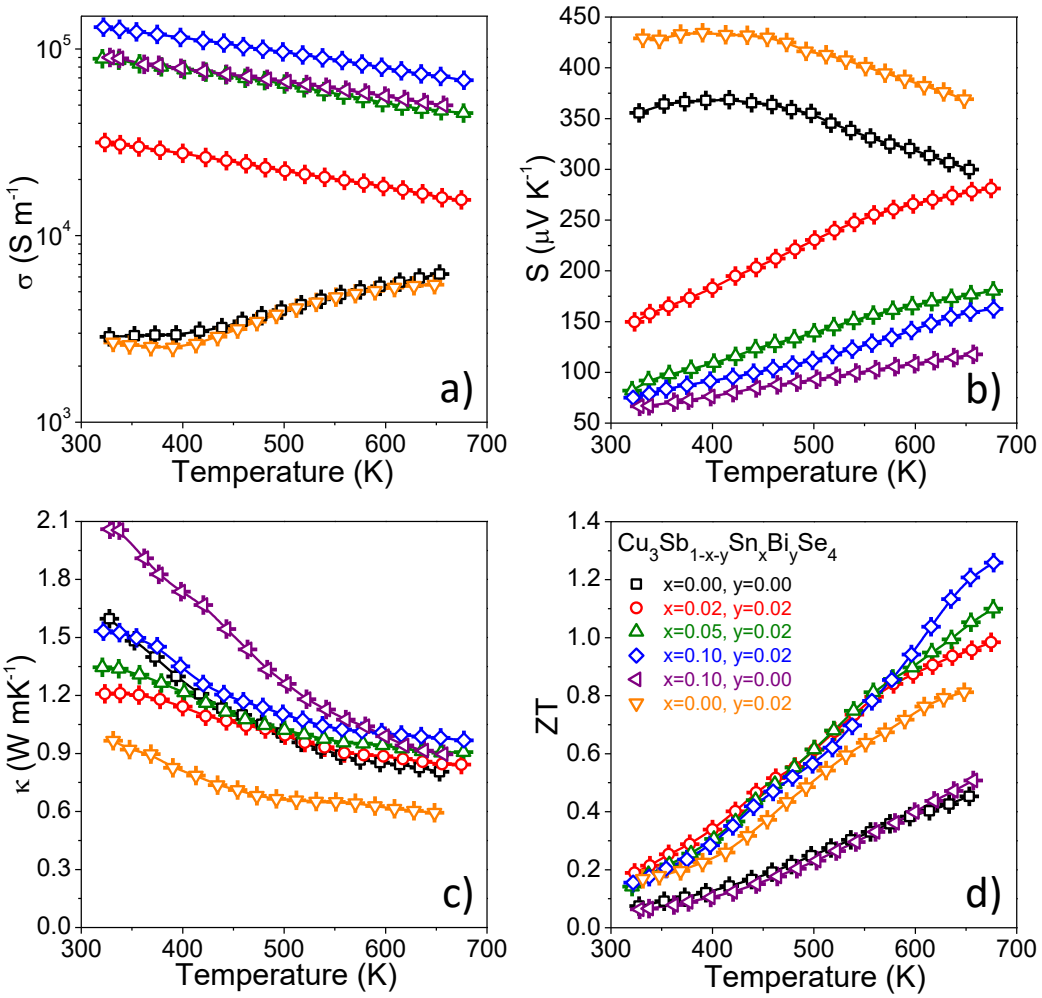

Figure 7. Temperature dependence of (a) electric conductivity (σ), (b) Seebeck coefficient (S), (c) thermal conductivity (κ), and (d) The figure of merit (ZT) of $Cu_3Sb_{0.98-x}Sn_xBi_{0.02}Se_4$ (x = 0.02, 0.05 and 0.10).

These materials were further employed to fabricate simple TE generator prototypes with a ring architecture (Figure 8). Such design optimizes the thermal contact between the TE generator and the walls of a hot or cold pipe, and at the same time minimizes the module form factor and provides improved mechanical stability compared with conventional flat devices. In this architecture, rings with n and p type materials could be placed thermally in parallel and electrically in series to harvest a radial heat flux (Figure 8a). Alternatively, multiple n and p elements could be integrated within each ring (Figure 8d). The module, containing multiple n- and p-type rings or several multi-element rings make use of a thin thermal and electrical insulator between rings and metal pins to alternatively contact the outer and inner rings as shown in Figure 8a. Single p-type $Cu_3Sb_{0.88}Sn_{0.10}Bi_{0.02}Se_4$ rings, with inner and outer diameter of 28 mm and 39 mm, respectively with copper thicknesses of 4 mm and thus a CASe thickness of 3 mm were assembled and tested in a custom made set-up as detailed in the experimental part (Figure 8b). The temperature of the tube was raised up to 250 ºC while maintaining a low temperature in the outside part of the rings. Figure 8c shows the voltage obtained from a single p-type

ring as a function of the temperature gradient. Open circuit voltages close to 20 mV were obtained for a single TE element exposed to a temperature gradient of 160 ºC. Being the electrical resistance of the ring 0.4 Ω, this voltage translates into a 1 mW of generated electric power for each single TE element. The combination of several TE p-n pairs in each ring (Figure 8d) and of several rings into a module (Figures 8e) could provide electric powers on the order of 100 W for 200-300 ºC temperature gradients as those available among other in exhaust gas pipes of vehicles with combustion engines.

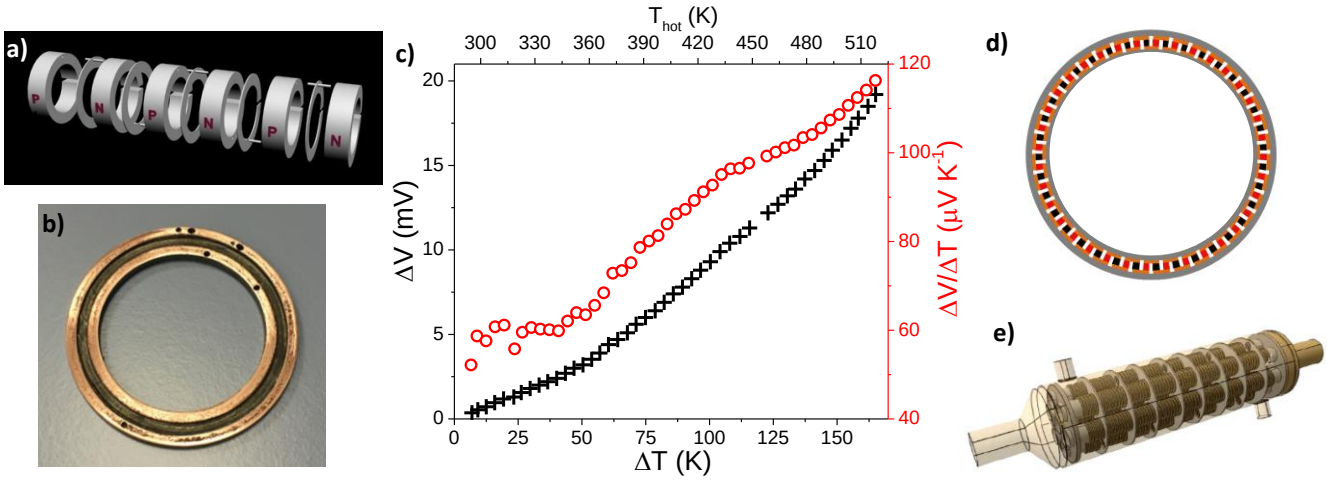

Figure 8. a) Scheme of a basic ring-based TE module, b) $Cu_3Sb_{0.88}Sn_{0.10}Bi_{0.02}Se_4$-based ring, c) Voltage obtained from a single $Cu_3Sb_{0.88}Sn_{0.10}Bi_{0.02}Se_4$ ring as a function of the temperature gradient when increasing the temperature at the hot side and maintaining the cold side at around ambient temperature. The hot side temperature is also displayed on the top axis. Red open circles display the apparent Seebeck coefficient of the ring. d) Scheme of a ring with multiple p and n type elements (in black and red). e) Scheme of a multi-ring system to be coupled to a hot pipe including a jacket for cooling fluid circulation.

4. CONCLUSION

In summary, a novel solution-based strategy to produce monodisperse CASe NCs at the gram scale was presented and the effect of Sn- and Bi-doping on the TE performance of CASe nanomaterials obtained via hot press were detailed. Sn was demonstrated to be a p-type dopant which effectively helped to control charge carrier concentration. On the other hand, the introduction of Bi conveniently modified the energy band structure of the compound resulting in higher S values. Besides, the introduction of any of the impurities helped to reduce the material lattice thermal conductivity. By optimizing the amount of Sn in a Bi-doped material, ZT values up to 1.26 at 673 K were obtained for $Cu_3Sb_{0.88}Sn_{0.10}Bi_{0.02}Se_4$, which is among the best ZT values obtained with a Pb- and Te-free material in this middle temperature range, with the additional advantage of the high versatility and low cost associated to solution processing technologies. Taking advantage of this processability, the innovative ring-shaped TE generators produced provided 1 mW of electric power per TE element with a 160 ºC

temperature gradient. The simple design and good thermal contact provided by the ring design and the low cost of the material and processes used potentially results in TE systems with short payback times.

ACKNOWLEDGEMENTS

This work was supported by the European Regional Development Funds, the Framework 7 program under project UNION (FP7-NMP-2012-310250) and the Spanish MINECO Project BOOSTER (ENE2013-46624-C4-3-R). YL thanks the China Scholarship Council (CSC 201406500003) for scholarship support. MI and SO thank AGAUR for their Beatriu de Pinós postdoctoral grant (2013 BP-A00344) and PhD grant, respectively. JDR thanks the FWO (Research Foundation Flanders) for financial support. M. V. K. acknowledges partial financial support by the European Union (EU) via FP7 ERC Starting Grant 2012 (Project NANOSOLID, GA No. 306733). JM Song acknowledges financial support by Natural Science Foundation of Anhui Province (Grant No. 1508085MB22). Authors also acknowledge the funding from Generalitat de Catalunya 2014 SGR 1638. MI and JCM thank the FWO MULTIMAR scientific research network for financial support for a short research stay. The 500 MHz used in this work was funded by the Hercules foundation (AUGE009/06).

REFERENCES

1. M. Yuan, D. B. Mitzi, W. Liu, A. J. Kellock, S. J. Chey and V. R. Deline, *Chem. Mater.*, 2009, **22**, 285-287.
2. Y. Zhao and C. Burda, *Energy. Environ. Sci.*, 2012, **5**, 5564-5576.
3. D. Aldakov, A. Lefrançois and P. Reiss, *J. Mater. Chem. C*, 2013, **1**, 3756-3776.
4. F.-J. Fan, L. Wu and S.-H. Yu, *Energy. Environ. Sci.*, 2014, **7**, 190-208.
5. A. Singh, A. Singh, J. Ciston, K. Bustillo, D. Nordlund and D. J. Milliron, *J. Am. Chem. Soc.*, 2015, **137**, 6464-6467.
6. W. Van Der Stam, A. C. Berends and C. de Mello Donega, *ChemPhysChem*, 2016.
7. M. Ibáñez, D. Cadavid, R. Zamani, N. García-Castelló, V. Izquierdo-Roca, W. Li, A. Fairbrother, J. D. Prades, A. Shavel and J. Arbiol, *Chem. Mater.*, 2012, **24**, 562-570.
8. J. Shi, Z. Li, D. Zhang, Q. Liu, Z. Sun and S. Huang, *Progress in Photovoltaics: Research and Applications*, 2011, **19**, 160-164.
9. X. Yu, X. An, A. Shavel, M. Ibanez and A. Cabot, *J. Mater. Chem. A*, 2014, **2**, 12317-12322.
10. A. Chirilă, S. Buecheler, F. Pianezzi, P. Bloesch, C. Gretener, A. R. Uhl, C. Fella, L. Kranz, J. Perrenoud and S. Seyrling, *Nat. Mater.*, 2011, **10**, 857-861.
11. A. Shavel, D. Cadavid, M. Ibanez, A. Carrete and A. Cabot, *J. Am. Chem. Soc.*, 2012, **134**, 1438-1441.
12. A. Carrete, A. Shavel, X. Fontané, J. Montserrat, J. Fan, M. Ibáñez, E. Saucedo, A. Pérez-Rodríguez and A. Cabot, *J. Am. Chem. Soc.*, 2013, **135**, 15982-15985.
13. A. Shavel, M. Ibáñez, Z. Luo, J. De Roo, A. Carrete, M. Dimitrievska, A. Genç, M. Meyns, A. Pérez-Rodríguez and M. V. Kovalenko, *Chem. Mater.*, 2016, **28**, 720-726.
14. X. Yu, A. Shavel, X. An, Z. Luo, M. Ibanez and A. Cabot, *J. Am. Chem. Soc.*, 2014, **136**, 9236-9239.
15. V. Lesnyak, C. George, A. Genovese, M. Prato, A. Casu, S. Ayyappan, A. Scarpellini and L. Manna, *ACS nano*, 2014, **8**, 8407-8418.
16. L. Shi, P. Yin, H. Zhu and Q. Li, *Langmuir*, 2013, **29**, 8713-8717.
17. M. Ibáñez, R. Zamani, A. LaLonde, D. Cadavid, W. Li, A. Shavel, J. Arbiol, J. R. Morante, S. Gorsse and G. J. Snyder, *J. Am. Chem. Soc.*, 2012, **134**, 4060-4063.
18. L. I. Berger, *Ternary Diamond-Like Semiconductors/Troinye Almazopodobnye Poluprovodniki/Тройные Алмазоподобные Полупроволники*, Springer Science & Business Media, 2012.
19. T.-R. Wei, H. Wang, Z. M. Gibbs, C.-F. Wu, G. J. Snyder and J.-F. Li, *J. Mater. Chem. A*, 2014, **2**, 13527-13533.
20. C. Yang, F. Huang, L. Wu and K. Xu, *J. Phys. D: Appl. Phys.*, 2011, **44**, 295404.

21. L. I. Berger and V. D. Prochukhan, 1969.
22. X. Pang, L. Zhao, W. Han, X. Xin and Z. Lin, *Nat. Nanotechnol*., 2013, **8**, 426-431.
23. J. Chang and E. R. Waclawik, *RSC Advances*, 2014, **4**, 23505-23527.
24. J. van Embden, A. S. Chesman and J. J. Jasieniak, *Chem. Mater.*, 2015, **27**, 2246-2285.
25. D. V. Talapin, J.-S. Lee, M. V. Kovalenko and E. V. Shevchenko, *Chem. Rev.*, 2009, **110**, 389-458.
26. M. Ibáñez, R. Zamani, S. Gorsse, J. Fan, S. Ortega, D. Cadavid, J. R. Morante, J. Arbiol and A. Cabot, *ACS nano*, 2013, **7**, 2573-2586.
27. M. Ibáñez, Z. Luo, A. Genç, L. Piveteau, S. Ortega, D. Cadavid, O. Dobrozhan, Y. Liu, M. Nachtegaal and M. Zebarjadi, *Nat. Commun.*, 2016, **7**.
28. J. van Embden and Y. Tachibana, *J. Mater. Chem.*, 2012, **22**, 11466-11469.
29. J. van Embden, K. Latham, N. W. Duffy and Y. Tachibana, *J. Am. Chem. Soc.*, 2013, **135**, 11562-11571.
30. K. Ramasamy, H. Sims, W. H. Butler and A. Gupta, *Chem. Mater.*, 2014, **26**, 2891-2899.
31. K. Chen, J. Zhou, W. Chen, P. Zhou, F. He and Y. Liu, *Part. Part. Syst. Charact.*, 2015, **32**, 999-1005.
32. D. Li, R. Li, X.-Y. Qin, C.-J. Song, H.-X. Xin, L. Wang, J. Zhang, G.-l. Guo, T.-H. Zou and Y.-F. Liu, *Dalton Trans.,* 2014, **43**, 1888-1896.
33. Y. Wu, X. Qiao, X. Fan, X. Zhang, S. Cui and J. Wan, *J. Nanopart. Res.*, 2015, **17**, 1-7.
34. M. A. Connell, P. J. Bowyer, P. A. Bone, A. L. Davis, A. G. Swanson, M. Nilsson and G. A. Morris, *J. Magn. Reson.*, 2009, **198**, 121-131.
35. D. Sinnaeve, *Concepts in Magnetic Resonance Part A*, 2012, **40**, 39-65.
36. Z. Hens and J. C. Martins, *Chem. Mater.*, 2013, **25**, 1211-1221.
37. J. De Roo, K. De Keukeleere, Z. Hens and I. Van Driessche, *Dalton Trans.*, 2016.
38. B. Fritzinger, I. Moreels, P. Lommens, R. Koole, Z. Hens and J. C. Martins, *J. Am. Chem. Soc.*, 2009, **131**, 3024-3032.
39. R. Dierick, F. Van den Broeck, K. De Nolf, Q. Zhao, A. Vantomme, J. C. Martins and Z. Hens, *Chem. Mater.*, 2014, **26**, 5950-5957.
40. Y. Li, X. Qin, D. Li, X. Li, Y. Liu, J. Zhang, C. Song and H. Xin, *Rsc Adv.*, 2015, **5**, 31399-31403.
41. X. Li, D. Li, H. Xin, J. Zhang, C. Song and X. Qin, *J. Alloy. Compd.*, 2013, **561**, 105-108.
42. S. M. L. I. Berger, CRC Press, Boca Raton, FL, , 1997, p. 267.
43. Z. K. A. Pfitzner, 1995, **209**, 685–685.
44. F. Tran and P. Blaha, *Phys. Rev. Lett.*, 2009, **102**, 226401.
45. D. Koller, F. Tran and P. Blaha, *Phys. Rev. B*, 2012, **85**, 155109.
46. D. Koller, F. Tran and P. Blaha, *Phys. Rev. B*, 2011, **83**, 195134.
47. Y. Zhang, L. Xi, Y. Wang, J. Zhang, P. Zhang and W. Zhang, *Comput. Mater. Sci.*, 2015, **108**, 239-249.